Capillary-pressure saturation relation derived from the pore morphology method

Fernando Alonso-Marroquin* and Martin P. Andersson
CIPR, King Fahd University of Petroleum and Minerals, Dhahran 31261, Kingdom of Saudi Arabia

(Received 13 January 2025; accepted 19 May 2025; published 16 June 2025)

A computationally efficient method to calculate the capillary pressure-saturation relations of immiscible multiphase flow on two-dimensional pore morphologies is presented. The method is an extension of the porous morphology method that includes the wetting angle and trapped mechanism of the displaced fluid, and calculation of material properties using density functional theory. After the method was validated with microchip fluid injection experiments, it was used to relate pore morphology to the capillary pressure-saturation relation using square-lattice pore morphologies. Because the method uses only morphological binary operations, it is more efficient than well-established high-resolution voxel dynamics methods such as lattice-Boltzmann methods and level-set computational fluid dynamics. Apart from pore morphology, only the material parameters related to the contact angle (wettability) and interfacial tension are required to connect the pore-saturation relation and pore throat distribution. We investigate the effects of interfacial tension, wettability, sample size, and pore throat distribution on entry pressure and residual saturation.

DOI: 10.1103/1dw6-m4v2

I. INTRODUCTION

The displacement of a fluid by another in porous media such as soils, rocks, and engineering materials is a complex process that is difficult to tackle from first principles. A common simplification is to assume that fluids are immiscible and incompressible, so that the process is governed by pore morphology and fluid properties, such as interfacial tension, wettability, and viscosity [1]. The original Lucas-Washburn model set the mathematical basis of the process [2], and closed-form solutions are available for uniform cylindrical geometries, accounting for the effects of dynamics [3], temperature [4], and multicomponents [5]. For more complex geometries, first-principles solutions are not available in analytical forms. The pressure-saturation relation is often used to characterize the invasion process. Initially, the porous medium is fully saturated by a resident fluid, then an invasive fluid is injected, and the saturation of the invaded fluid is measured. This process is performed in a quasistatic fashion; thus, it is expected that viscous forces play a minor role, and the invasion process is governed by capillary forces at the fluid interfaces. In addition to its importance in understanding the fluid flow through a porous medium, the capillary pressure-saturation relationship is also one of the key inputs in reservoir scale simulation, and therefore efficient simulation of the pressure-saturation relation can also serve as a key component in scaling up molecular- and pore-scale phenomena to the field scale, via reservoir simulations.

Due to the exceptional growth of computational power, fluid invasion is often simulated using computationally intensive voxel dynamics methods, such as the lattice-Boltzmann method [6,7] and level-set computational fluid dynamics [8]. Less attention has been paid to more efficient quasistatic methods, such as the Pore Morphology Method, where the quasistatic invasion is modeled by simpler morphological operations [9]. Voxel dynamics simulations are computationally expensive; a single simulation on 1000^3 voxels requires millions of time steps to run on supercomputers. Quasistatic binary algorithms are more favorable than voxel dynamics algorithms, since they do not pose time step instabilities and involve many fewer computational operations.

In this paper, we exploit the advantages of the Pore Morphology Method to calculate the quasistatic response of the saturation due to the increase in capillary pressure in an extremely efficient way. Technically, we are treating a drainage process, because the defending fluid is the wetting phase throughout the paper. Our starting point is the original Hilper and Miller algorithm [9]. In their method, the saturation at a given pressure is calculated by performing mathematical morphology operations and connectivity functions on the binarized pore image. Here, we extend the method to account for the trapped mechanism: resident fluid that gets disconnected from the evacuation zone is considered trapped, so that the invasion is forbidden there. The extended Pore Morphology Method is presented in Sec. II. The material constants involved in the simulations are given in terms of interfacial tensions that are calculated using the density functional theory (DFT) in Sec. III. The method is validated by comparison with two-dimensional (2D) microchip experiments in Sec. IV. In Sec. V, we present the dimensional analysis of the pressure-saturation relation and perform numerical simulations on square lattices to investigate the effects of material and geometric heterogeneity on the pressure-saturation relations. We also investigate finite-size effects to determine whether the pressure-saturation relations hold in the statistical limit where the sample is large enough to become a representative element for large-scale reservoir simulation. Sections VI and VII are devoted to the discussion of results and overall conclusions.

*Contact author: fernando.marroquin@kfupm.edu.sa

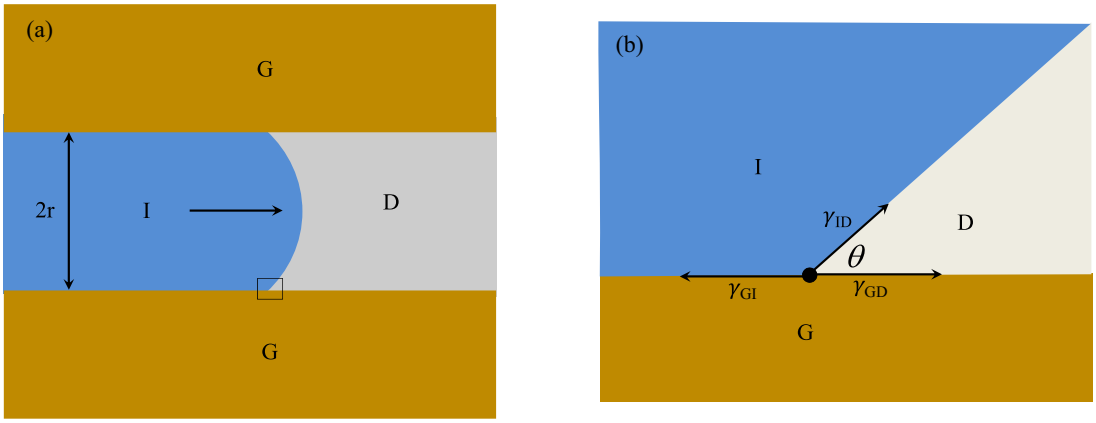

FIG. 1. (a) Representation of a fluid (I) invading a second fluid (D) in a pore throat of radius r. The two phases intersect the solid granulate (G) at the contact line/curve. (b) Balance of linear tensions (force per unit of length), or equivalently, interfacial free energies (energy per unit area) at the contact line.

II. PORE MORPHOLOGY METHOD

Consider an incompressive resident fluid that completely fills a porous medium. Then, an invasive fluid is injected in a given region of the porous medium. The medium is defined as a binary partition of a subset $S \subset \boldsymbol{R}^2$ of the Euclidean space into a granular matrix G and a void space V; that is, $G \cup V = S$ and $G \cap V = \emptyset$. The void space is initially filled with resident fluid that can escape through an *evacuation* zone $E \subset V$. The invading fluid is injected into the void space through a region $R \subset V$ that we call the *reservoir*. Invasive fluid displaces resident fluid in an immiscible manner by the action of capillary pressure ΔP_c. The *invaded* fluid is labeled I while the resident fluid is named *defensive* fluid and labeled D. The invasion process is governed by the equilibrium equation of the contact line/curve where the three phases intersect [10] [see Fig. 1(b)]

$$\gamma_{GD} - \gamma_{GI} = \gamma_{ID} \cos\theta, \tag{1}$$

where γ_{GD}, γ_{GI}, and γ_{ID} are the interfacial tensions between granular-defensive fluids, granular-invasive fluids, and invasive-defensive fluids. The variable θ is the *contact angle*, often referred to as the wetting angle in the literature [1]. The free-body diagram of the contact interface is shown in Fig. 1(b). Let us define ΔP_c as the capillary pressure at the fluid-fluid interface. The capillary pressure threshold for invading a throat of radius r is obtained by balancing the forces along the throat [see Fig. 1(b)]. The component of force at the interface S along the throat is $F = \int_S \Delta P_c dS cos\alpha$, where α is the angle between the normal unit vector at the interface and the throat direction. Since the capillary pressure is constant, $F = \Delta P_c \int_S dS cos\alpha = \Delta P_c \times area = \Delta P_c 2rd$, where d is the depth of the sample. The tension due to the capillary forces is $T = \gamma_{ID} \times perimeter \times \cos\theta = \gamma_{ID}(2r + d)\cos\theta$. Balancing these forces, $(F = T)$ leads to the Young-Laplace equation

$$\Delta P_c = 2\gamma \cos\theta \left(\frac{1}{2r} + \frac{1}{d}\right), \tag{2}$$

where $\gamma = \gamma_{ID}$ is introduced to simplify the notation. We also remove the contribution of the out-of-plane surface tension by defining the effective capillary pressure as $P_c = 2\gamma \cos\theta/d + \Delta P_c$. Thus, the Young-Laplace equation given by Eq. (2) reduces to

$$r = \frac{\gamma \cos\theta}{P_c}. \tag{3}$$

For a given capillary pressure P_c, Eq. (3) defines the radius of all throats that can be potentially invaded. This radius is defined here as the *capillary radius*, and is treated as the control parameter in our simulations.

The original algorithm of Hilper and Miller [9] calculates the invaded pore space in terms of capillary radius using connectivity functions and mathematical morphological operations on binary images. The Hilper and Miller algorithm does not have a trapped mechanism. For a capillary radius r, the zone reached by the invading fluid is calculated as $I_r = C(I \ominus \hat{S}_r, R) \oplus \hat{S}_r$, where $\hat{S}_r = S_r \cup S_{r-1}$, and S_r is the digital sphere of radius r. The function $A = C(B, R)$ returns the connected component of the image B that is connected to the image R [9].

Here, we present a modification of the algorithm that considers a trapped mechanism: any evacuating fluid that is completely surrounded by the invaded fluid is assumed to be trapped. In our algorithm, the void space V is partitioned into a defended zone D, an invaded zone I, and a trapped zone T. Initially, the capillary radius is set to the largest throat neck of the void space, then the capillary radius is progressively reduced, and the invaded zone is calculated. The trapped zone is added when any part of the defended zone gets disconnected from the evacuation area. The initial conditions in the simulation are $D = V$, $I = T = \emptyset$. To update these zones, we use the same connectivity function $A = C(B, R)$ of the Hilper and Miller algorithm. We define the complement of a subset $A \subset V$ of the void space as $A' = V - A$. Based on these functions, the steps of the simulation loop are as follows:

(1) The void image is morphologically eroded with a sphere S_r of radius r, resulting in $I_{ero} = V \ominus S_r$.

(2) The part of I_{ero} that is not trapped and is connected to the reservoir is dilated: $I_{new} = C(I_{ero} \cap T', R) \oplus S_r$. Remove

any trapped area from this set $I_{\text{new}} = I_{\text{new}} \cap T'$. Then, this set is added to the invaded zone: $I = I \cup I_{\text{new}}$.

(3) The defended area is calculated as the void space that is not invaded and is connected to the evacuation area $D = C(V \cap I', E)$.

(4) The new trapped zone is the void space that is neither in the defended zone nor in the invaded zone $T_{\text{new}} = V \cap D' \cap I'$. This area is added to the trapped zone: $T = T \cup T_{\text{new}}$.

(5) The capillary radius is decreased ($r \to r - 1$); return to step 1 unless $r = 0$.

The algorithm is an improved version of the Hilper and Miller method that allows the trapping mechanism and reduces to the nontrapping pore invasion method of the Hilpert and Miller algorithm when $E = V$. The algorithm is numerically more efficient than voxel-dynamics-based solvers such as the lattice-Boltzmann method or the level-set method. This is because the operations in the Pore Morphology method are binary rather than floating-point calculations. Since the algorithm is quasistatic, it does not have a time step numerical error. Instead, the origin of the numerical error is in the pixel size (image resolution). The method does not account for viscous effects, but this is a point in our favor, as we aim to focus solely on capillary effects. A stand-alone Matlab implementation of the algorithm is included in the Supplemental Material [11].

Having the calculations of throat sizes is convenient to initialize the capillary radius and to further accelerate the algorithm. To obtain the list of throat sizes, a pore network extraction is needed. This procedure is based on the segmentation of the void space into pores; each pore is connected to the other by throats. Then, the interconnected pores can be represented by a pore network, or more precisely, an undirected graph. The graph itself can be seen as an image where the pores are treated as superpixels and the throats are treated as connections between the superpixels. The morphological operations and connectivity functions can be rewritten to operate on these graphs in more efficient code that is pixel-independent. Besides, the number of operations is much lower since the number of superpixels corresponds to the number of pores, a number that is much lower than the number of pixels in the binary image.

To extract the pore network, we perform a workflow algorithm that we call *charting* of the pore space. First, we calculate two quantities from the binary image of B the void space: the label matrix L and the skeleton κ. The label image L is calculated from B by applying the standard watershed segmentation on the void space using the city-block distance transform. The skeleton κ reduces the binary image into a 1-pixel-wide curved lines, while preserving the topology and Euler number of the image. From the skeleton, we identify the branch points. These points connect different branches of the skeleton. Domains of L that do not contain branch points of the skeleton are considered invalid pores and are labeled zero in the label matrix. Then, a gray dilation algorithm is used to assign to the pixels of the invalid pores that are not resolved by the watershed segmentation. The techniques of this procedure are explained by Rabbani *et al*. [12]. The charted pore space defines the pores as the domains of the final label matrix L, and the throats as the interfaces between the pore domains from where the throat radii are calculated.

TABLE I. Density functional theory calculation of interfacial free energy (mN/m) using COSMO-RS. Oil corresponds to FC43 and solid to polydimethylsilane. The experimental water-oil surface tension is taken as 55 mM/m, and the experimental contact angle is curve-fitted as $\theta_0 = (55 \pm 5)^o$ by Yiotis *et al*. [8].

Water-oil	Water-solid	Oil-solid	Weight factor
47.6	11.6	9.9	excluding edge-bridging 0s
	17.9	9.8	including one edge-bridging 0
	50.6	9.7	including only CH3 and Si
	53.1	9.6	including only CH3 groups
Average			
47.6	33.3	9.7	contact angle: 60°

III. MOLECULAR MODELING

The material properties (contact angle and interfacial tension) are calculated using DFT. To demonstrate the potential of scaling up the results of molecular modeling to relevant phenomena at the pore scale, we calculated the liquid-liquid interfacial tension [13] and the contact angle [14] for our comparison to microchip experiments [8]. Although experimental results for the contact angle are available for this particular system, there are systems in which experimental results do not exist or are difficult to obtain. In such cases, molecular modeling can provide an estimate of the contact angle required to model the pore scale and multiphase flow properties, and therefore, the combined multiscale approach is used here to demonstrate an integrative approach also applicable to such more difficult systems.

The experiments were carried out using a solid polydimethylsilane (PDMS), deionized water as the invading fluid, and the FC43 polyfluorinated liquid as the defending fluid. We used Turbomole v7.8 [15], the BP functional [16,17], the TZVP basis set [18], and the implicit solvent model of COSMO [19] for DFT calculations of the surface energies of the constituents. All DFT calculations were performed using COSMOtherm, the BP_TZVP_C30_1601.ctd parametrization [20] and the scripts detailed in Ref. [14]. We modeled the PDMS surface using a dimethylsilane pentamer, with the end monomers removed in the COSMOtherm calculations, a standard method for treating polymers using COSMO-RS. The results were averaged for weight factors with and without including the oxygens in the backbone of the PDMS molecule. This was done because the oxygens in the silane backbone are located deeper from the surface and do not have full access to the fluid in contact. The methyl groups are located farther out of the backbone and would be in contact with the fluid. Therefore, they were always included in the DFT calculations. The DFT calculations predicted the liquid-liquid interfacial tension between water and FC43 as well as the solid-liquid interfacial tensions between the PDMS solid surface and water and between PDMS and FC43. The contact angle was then calculated using Young's equation [Eq. (1)]. Free surface energies are interpreted as interfacial tensions. The calculated free energies are presented in Table I. The different assumptions made about molecular interactions in the calculations resulted in a significant variation in the individual water-solid interfacial tensions. However, the average value

yielded a contact angle in agreement with the curve fitting used in the experiments [8]. We would interpret this in the sense that water has a difficult time reaching the deep-lying oxygen atoms of the backbone of the PDMS, and therefore, the water molecules are only partially in contact with this part of the molecular surface. Thus, the average interfacial tension that includes both a molecular surface with and without the backbone oxygen atoms in the PDMS gives a result in agreement with experiments. We note that the DFT + COSMO-RS calculations used to predict the contact angle and interfacial tensions took about 1 hour on a multicore PC. They are thus significantly more computationally expensive than the pore morphology simulations, but since the DFT calculations are not coupled with the pore morphology simulation, they do not add computational bottlenecks.

IV. COMPARISON WITH MICROCHIP EXPERIMENT

To validate the numerical method, we compare it with the two-dimensional experiment reported by Yiotis *et al*. [8]. The micromodel consists of a rectangular area that is 6 mm long and 4 mm wide. It also includes two flow channels that are 13 mm long and 500 μm wide, connected to liquid buffers. The micromodel is 115 μm deep and contains 76 nonoverlapping cylindrical pillars with an average diameter of 380 μm. FC43 Oil is used as the wetting (defensive) fluid and water as a nonwetting (invaded) fluid. The pressure sensor has a maximum pressure reading of 7000 Pa and a typical precision of 20 Pa. Water is pumped on one side of the chip through a tube of diameter 1 *mm*, and the oil is evacuated on the other side through a tube of the same diameter. The water is injected with a constant flow rate of 10^{-4} ml/min. The value of the interfacial tension reported in the experiment is $\gamma = 55\,\mathrm{N/m}$. The contact angle of $\theta_0 = 60^0$ was calculated based on DFT using COSMO-RS software. The computed value gave very consistent results for the pressure-saturation relation.

We capture the distribution of both the wetting and nonwetting phases each time the pressure reaches a maximal value and a new pore is invaded. Then, the capillary radius is recorded as $r = \gamma \cos\theta_0 / P_c$ at the point of maximal pressure. In the pore morphology simulation, the capillary radius is initialized with a value larger than the largest throat. Then, in each simulation step, the capillary radius is reduced by one pixel, and the invaded and trapped areas are calculated using the pore morphology algorithm described previously. The first step is to calculate the morphological erosion of the void space by a sphere of radius r, the capillary radius, as shown in the first line of Fig. 2. In the original Hilper and Miller algorithm, the eroded space that is connected to the injection area is morphologically dilated, and the dilated space corresponds to the invaded zone, shown in the second line of Fig. 2. The Hilper and Miller algorithm returns the saturation as a function of pressure, or capillary radius, but since there is no trapping mechanism for the defensive fluid, the saturation of the wetting phase reaches zero as the pressure increases (i.e., the capillary radius reaches zero).

Our modified pore morphology method accounts for trapped wetting fluid by adding an additional rule: In each step, the defending fluid that gets disconnected from the evacuation area is added to the trapped zone. The numerical results of this modified algorithm are shown in the third line of Fig. 2. The initial trapped zones are relatively small and appear as menisci of resident fluids. Near the breakthrough point, large zones of wetting fluid get trapped, and at the end of the simulation, the saturation of the wetting fluid reaches a residual value. We compare the invasion pattern with the experimental results shown in the fourth line of Fig. 2. A perfect match is observed below the breakthrough point, and there are significant differences in the final stage. In the flow-controlled experiment, a viscous finger reaches the breakthrough that produces a larger residual saturation than in the pressure-controlled simulation. This discrepancy is expected because the experiment is flow-controlled, so the capillary radius can increase during injection. However, the simulations are pressure-controlled so that the capillary radius always decreases. The simulations are expected to reproduce the pressure-saturation relation when the pressure is quasistatically increased and the saturation is measured. The experiment includes dynamics effects such as viscosity that are not taken into account in the simulations. However, it is reasonable to assume that viscous effects would be negligible in a quasistatic condition where the pressure is slowly increased and the saturation is recorded from the pressure-controlled experiments.

V. PORE MORPHOLOGY METHOD ON SQUARE LATTICES

In the previous section, the void space occupied by both wetting (resident) and nonwetting (invading) fluids was calculated by quasistatic simulations of pressure-controlled experiments by increasing the capillary pressure and hence decreasing the capillary radius, and calculating the regions occupied by the wetting and nonwetting fluids. In this section, we calculate the saturation of these fluids, which is defined as the percentage of void space occupied by each fluid. We focus on the variable S that is the saturation of the resident fluid (defensive), here referred to simply as *Saturation*. The pressure-saturation relation depends on the material parameters γ and θ, as well as the geometry and topology of the pore network of the void space.

To investigate the dependence of the pressure-saturation relation on these parameters, we concentrate on the simplest pore network topology, that is, the square lattice. Each pore in the square lattice is connected to its four neighbors by cylindrical throats. Radii throats are randomly generated with a log-normal distribution with median throat size $\tilde{r}$ and normal standard deviation σ. The contact angle θ is assumed to be uniformly distributed in the range $\theta \pm \Delta\theta$. As boundary conditions, the injection zone is the upper boundary of the rectangular sample, and the evacuation zone is the lower boundary.

Notice that the saturation will depend on the pore size distribution (PSD) of the square lattice. More precisely, the saturation should be obtained by adding the area of all invaded pores and dividing by the total void area. A simplified calculation of saturation is given by the fraction of invaded pores. We observe that in the statistical limit (i.e., for large enough samples or for averages over many samples), both calculations of saturation lead to similar results. Thus, the results reported

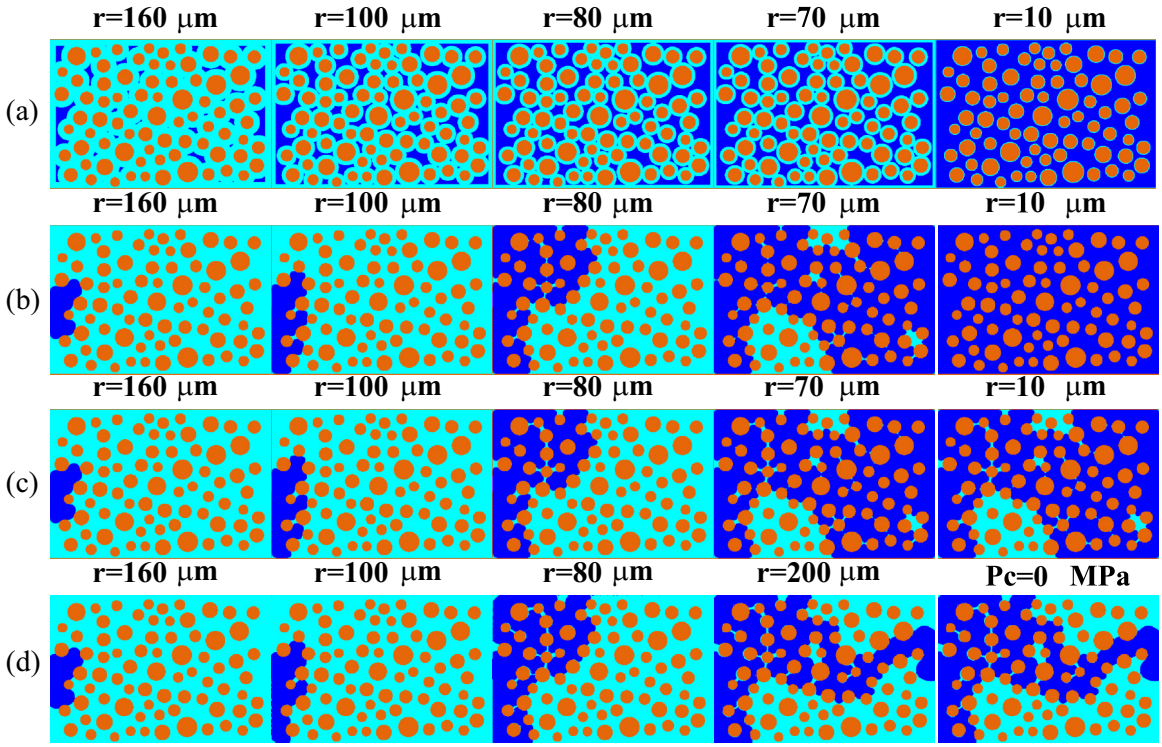

FIG. 2. Snapshots from flow-controlled experiment and pressure-controlled simulations for different capillary radii. The dark orange, blue, and green regions represent the granulate, invaded zones, and defended/trapped zones, respectively. The injection and evacuation zones each correspond to 10% of the domain's left and right boundaries. The capillary radius is given by $r = \gamma \cos\theta_0 / P_c$ so that increasing capillary pressure leads to a decrease in the capillary radius. The first and second columns correspond to the initial stages of invasion. The third and fourth columns show snapshots immediately before and after the breakthrough. The last snapshot is the final stage of the invasion. Snapshots in (a) show the morphological erosion of the void space by a disk or capillary radius r. Snapshots in (b) shows the pore morphology simulation results based on the original Hilper and Miller algorithm [9], without a trapping mechanism. In their algorithm, the zone invaded by the nonwetting fluid is calculated as the dilation of the eroded space in (a) that is connected to the reservoir. (c) Snapshots of our pore morphology simulation that accounts for the trapped mechanism: defended (nonwetting) fluid that loses contact with the evacuation zone gets trapped. (d) Snapshot of the flow-rate controlled experiments at the peaks of the capillary pressure; notice that at the end of the experiment, the pressure drops as the invasive fluid breaks through. The match between our simulation and experiments is perfect before the pressure peaks. Our pore morphology simulations do not capture the viscous fingering after pressure peaks, but they allow derivation of the pressure-saturation relation since the simulation is pressure-controlled and quasistatic.

in this paper used the simplified calculation of saturation as the fraction of invaded pores.

A. Dimensional analysis

The parameters of our simulation are classified as material, statistical, and geometrical parameters. Our simulations are quasistatic, hence, the viscosity is absent, and the only material parameters are the interfacial tension γ and the contact (wetting) angle θ. In certain cases where the granulate is heterogeneous, the contact angle can vary from point to point. A simplified description of the material heterogeneities requires two parameters that account for the mean value θ_0 and the standard deviation $\Delta\theta$ of the contact angle. The statistical parameters describe the geometrical heterogeneity of the pore network. Since the pore throats are log-normally distributed, we define $\tilde{r}$ as the median of the log-normal distribution and σ as the standard deviation of the normal distribution corresponding to the log-normal one. The geometric parameters are given by the average grain diameter $\bar{\ell}$ and the dimensions of the sample L_x and L_y. The default parameters are listed in Table II.

TABLE II. Parameters used in Pore Morphology simulations. In microchip simulation (MS), the porous geometry and material parameters are taken from the microchip experiment of Youtis *et al.* [8]. The fourth column is for the square-lattice (SL) simulations, listing the default parameters of the simulation using random throat distributions.

Variable	Symbol	MS	SL	Units
Interfacial tension	γ	55	50	mN/m
Mean contact angle	θ_0	60	50	Degrees
Contact angle dispersion	$\Delta\theta$	0	0	Degrees
Median throat radius	$\tilde{r}$	–	10	μm
σ-Parameter log-normal	σ	–	0.1	–
Average grain diameter	$\bar{\ell}$	380	100	μm
Sample length in x	L_x	6	4	mm
Sample length in y	L_y	4	4	mm
Graph/lattice	g	–	Square	–

The relation between the saturation of the defended (wetting) fluid S and the capillary pressure P_c in terms of the parameters of the model is

$$S = F_g(P_c, \gamma, \bar{r}, \sigma, \theta, \Delta\theta, \bar{\ell}, L_x, L_y), \tag{4}$$

where F_g is an unknown function for a given contact network g. Using dimensional analysis, it can be shown that the nondimensional saturation variable will depend on dimensionless variables only:

$$S = f_g(P_c\bar{r}/(\gamma\cos\theta_0), \sigma, \Delta\theta, L_x/\bar{R}, L_y/L_x). \tag{5}$$

From here, we obtain the dimensionless pressure in terms of dimensionless quantities,

$$\frac{P_c}{P_0} = \tilde{f}_g(S, \sigma, \Delta\theta, L_x/\bar{R}, L_y/L_x), \tag{6}$$

where,

$$P_0 = \frac{\gamma\cos\theta_0}{\tilde{r}}. \tag{7}$$

P_0 is the characteristic pressure, corresponding to the capillary entry pressure for a cylindrical tube of radius $\tilde{r}$. Equation (6) defines the functional relationship between dimensionless capillary pressure and saturation in terms of dimensionless parameters σ accounting for the variability of the pore throat radii, $\Delta\theta$ for the heterogeneity of the materials parameters of the granulate, $L_x/\bar{R}$ for the size of the network, and L_y/L_x for its aspect ratio.

We investigate here the parametric dependency of the function $\tilde{f}$ on these dimensionless variables.

B. Pressure-saturation relation

Here, we calculate the relation between the dimensionless pressure and saturation for the default parameters listed in Table II. First, we generate random contact networks; each network has the same topology of the square lattice, but the pore throat distribution (PTD) is randomly generated in each lattice. The results are shown in Fig. 3. We observe a strong statistical variation in the pressure-saturation relation. This variation is particularly significant when the sample reaches residual saturation. To obtain statistically representative results, we need to average the results over a large number of samples. The average pressure-saturation relationship shows an inflection point at $P = P_0$ that corresponds to the *entry pressure*. Below the entry point, the saturation changes little with any increase in capillary pressure. On the other hand, when $P_c > P_0$, the saturation decreases with an increase in pressure, and it asymptotically reaches a residual saturation.

The evolution of the pore invasion exhibits a behavior similar to other statistical processes such as bond percolation [21], backbone percolation [22], and invasion percolation [23] (see Fig. 4). The entry pressure P_0 resembles a critical percolation threshold, where the clusters of invaded fluid span over the size of the sample. A well-defined value near the entry pressure is observed in each sample, where the breakthrough occurs, and the saturation experiences a sudden decrease. Slightly above this percolation threshold, the zone of the invaded fluid produces a dense system of percolation paths that resembles the backbone percolation threshold [22]. For large

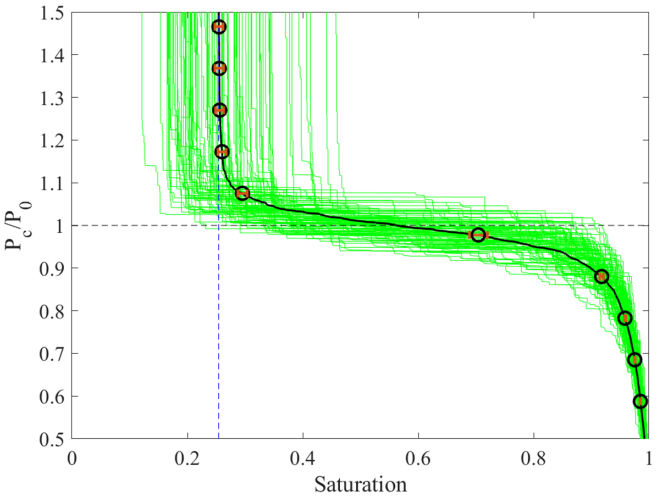

FIG. 3. Dimensional capillary pressure versus saturation of the wetting (defended) fluid. The green lines are the result for individual samples, and the black line is the average over all samples. The dashed horizontal line represents the entry pressure where $P_c = P_0$, and the dashed vertical line is the residual saturation. The error bars are obtained by averaging the results over 96 samples; the width of the error bars is the standard error.

pressures, the invasion process reaches a steady state where clusters of trapped fluid of all sizes are created. In addition, the final pattern of the trapped fluid is very sensitive to the initial seed of the random generation of the network. These features are typical of self-organized critical systems [24]. It is evident in Fig. 4 that large clusters appear on the boundaries, leading to boundary and finite-size effects. These effects are explored in Sec. V F.

C. Effect of surface and/or interfacial tension

In virtue of the dimensional analysis, the pressure-saturation relation in Fig. 3 is the same for arbitrary interfacial tensions γ and contact angles θ_0. We can recover the dimensionality by selecting these material parameters and plotting the dimensional capillary pressure against saturation. Figure 5 shows the curves for typical surface tension between mercury, air, water, oil, and hexane. An increase in surface tension leads to an increase in the entry pressure, while all pressure-saturation curves are self-similar, and they share the same residual saturation, that is, the residual saturation does not depend on the surface tension. We note that residual saturation may be affected by surface and interfacial tension in a real experiment. Our simulations demonstrate that, in the special case of pressure-controlled and quasistatic pore invasion in immiscible fluids, surface tension does not play a role in determining the residual saturation.

D. Effect of heterogeneity of pore network

For a given pore topology, such as the square lattice in our case, the statistical characterization is given by the PSD and PTD. PSD directly affects residual saturation, but in the statistical limit, the saturation can be given in terms of the fraction of invaded pores. The PTS affects the pressure-saturation

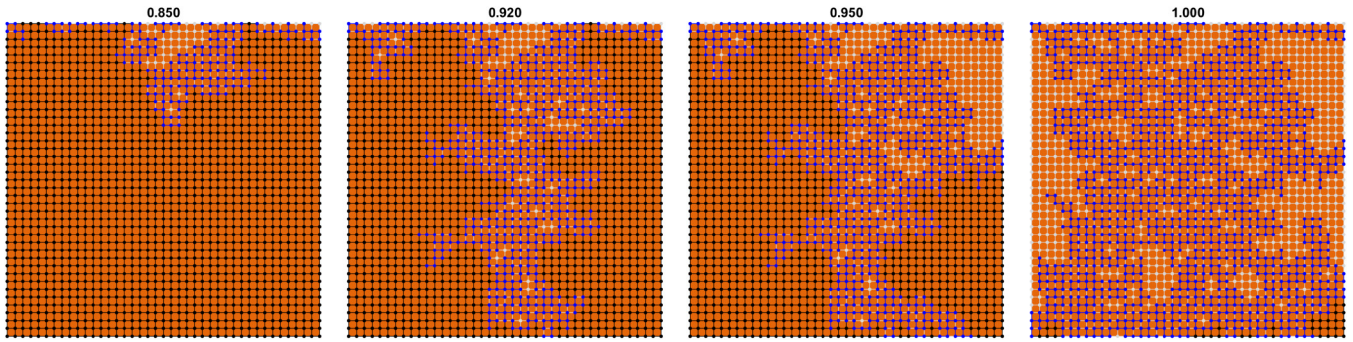

FIG. 4. Snapshot of pore invasion simulations. The numbers at the top are the values of P_c/P_0; the percolation transition occurs near $P_c = P_0$. The dark orange and black regions represent the granulate and defending fluid. The blue and light gray regions represent the invaded and trapped zones.

relation in two ways, the median of PTS $\tilde{r}$ is inversely proportional to the entry pressure, as shown in Eq. (7). The parameter of the standard deviation σ affect the pressure-saturation relation via Eq. (6). Here, we investigate the effect of the variance of the PTD.

Again, we can use the dimensional analysis to investigate the dependency of the pressure-saturation relation on the broadness of the PTD while fixing the other parameters. For a given parameter $\tilde{r}$ measuring the median of the PTD, the parameter P_0 is calculated using Eq. (7). Then, the relation between dimensionless pressure P_c/P_0 and saturation is calculated using Eq. (6). The results are shown in Fig. 6. The PDF median is fixed at $\tilde{r} = 10\,\mu\text{m}$ and the variance σ is changed. For all values of σ, the pressure-saturation relations share the same entry pressure and residual saturation. The effect of σ is on the sharpness of the transition around the entry pressure: if σ is small (narrow PTD), the transition is sharp and becomes smoother as σ increases (wider PTD).

E. Effect of heterogeneity of the granulate

The previous results account for the geometric heterogeneity of the pore network. It is also relevant to investigate how the pressure-saturation relationship depends on how heterogeneous the granular matrix is. Natural porous media such as sands and sandstones have different mineral compositions, typically including quartz, feldspar, heavy minerals, and cementing materials [25]. Carbonate rocks are composed mainly of calcite and dolomite [26]. Mineral composition directly affects wettability, so the contact angle θ is expected to vary from point to point on the granulate. The heterogeneity of the material is accounted for by the parameter $\Delta\theta$ that indicates how broadly the variance of the contact angle is distributed. The contact angle changes uniformly in the range $\theta_0 \pm \Delta\theta$. Figure 7 shows the dependence of the pressure-saturation relation on the dispersion of θ. We note that an increase in the variance of the contact angle distribution produces a decrease in the entry pressure and a smoother transition around the entry pressure. This comes from the lower values of θ present in the wider distribution, leading to a lower entry pressure (Fig. 5). The actual shape of the pressure-saturation curve does depend on the distribution, and for more quantitative results, a more realistic representation of the contact angle distribution would be warranted. Interestingly, all curves share the same residual saturation value, indicating that, again, the residual saturation does not depend on the variability of the contact angle.

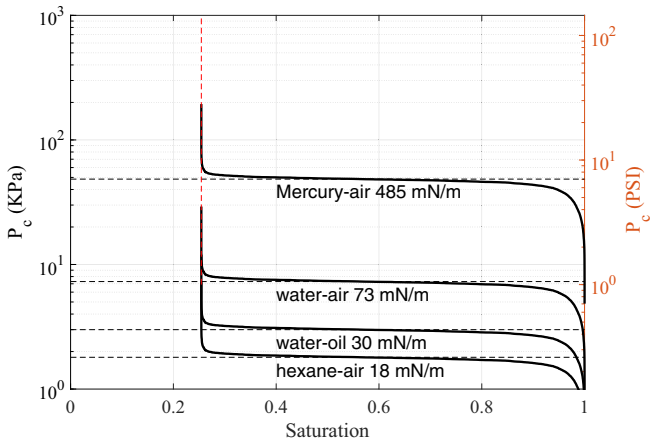

FIG. 5. Pressure-saturation relation for different surface and interfacial tensions. The units of pressure are given in SI units (left) and Engineering PSI units (right).

F. Finite-size effect

The results shown in the previous section were performed with a fixed sample dimension 4 mm × 4 mm with a grain diameter of 0.1 mm. Here we address the question of whether this sample is representative enough for using the pressure-saturation relation for large-scale simulations. In other words, we ask the following: How is the pressure-saturation relation affected by an increase in sample size? For this analysis, we fix the aspect ratio of the sample to one and change the sample dimensions. All other parameters are fixed.

The dependency of the pressure-saturation relationship on sample size is shown in Fig. 8(a). The entry pressure does not change with the sample size, but as the sample size increases, the transition around the entry pressure becomes sharper. The main effect of changing the size of the sample is the change in residual saturation; larger samples lead to higher residual saturation. It is also remarkable how slow the convergence of the residual saturation is as the sample size increases.

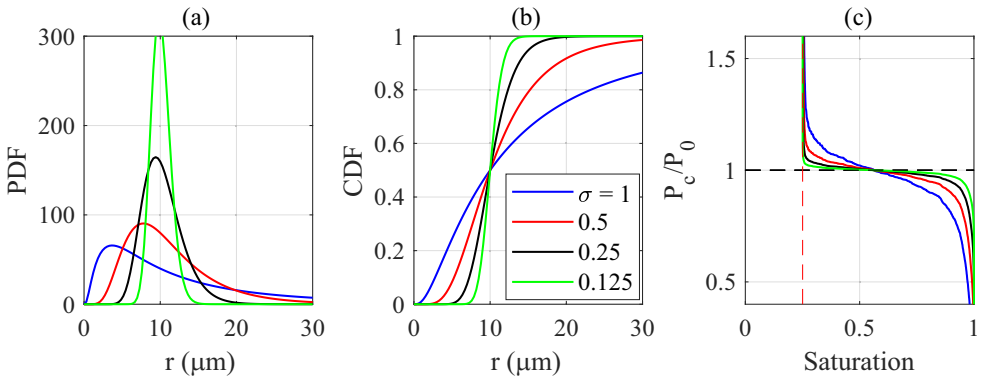

FIG. 6. (a) Different variances in the pore throat distributions with the same media $\tilde{r} = 10\,\mu$m. (b) Cumulative distribution of throat distributions. (c) Pressure-saturation relations for the different throat variances share the same entry pressure and residual saturation (dotted lines).

Simulations were performed with samples of $0.26m$, and we still did not achieve convergence of the residual saturation.

To estimate residual saturation for infinite samples and to verify convergence, we fit the dependency of residual saturation S_r to a power law. The fitting parameters are the residual saturation for infinite samples S_∞ and the power-law exponent α, that is, $S_r = S_\infty - (L_0/L)^\alpha$. The result of the power-law fit is shown in Fig. 8(b). We achieve a very good fitting except for very small samples, where the boundary effect may produce deviations from the power law. The power-law exponent is 0.26, indicating a very slow convergence of the residual saturation. The residual saturation for infinite samples is quite high, 55%. This is expected to be the characteristic value for square lattices, and it should depend on the lattice's topology and dimensionality.

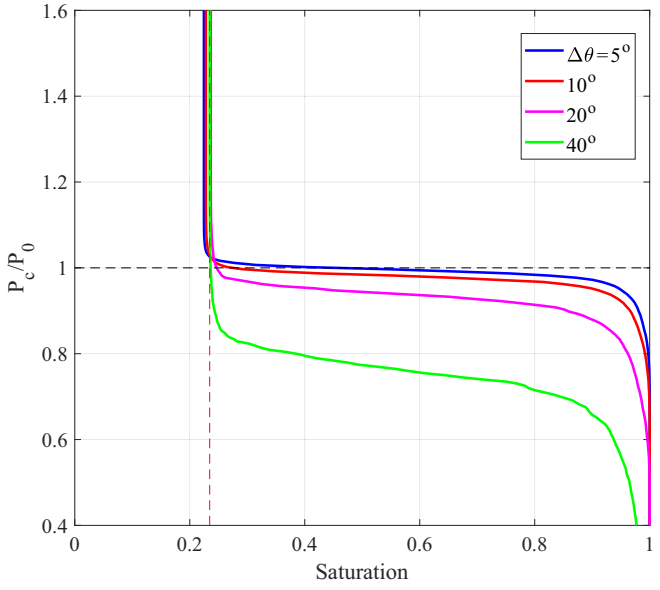

FIG. 7. Pressure-saturation relation with different variability of the contact angle. The curves do not share the same entry pressure, and vanish in the extreme case when $\Delta\theta = 40^0$. This is the case when the contact angle changes from 10^0 to 90^0. All curves share the same residual saturation.

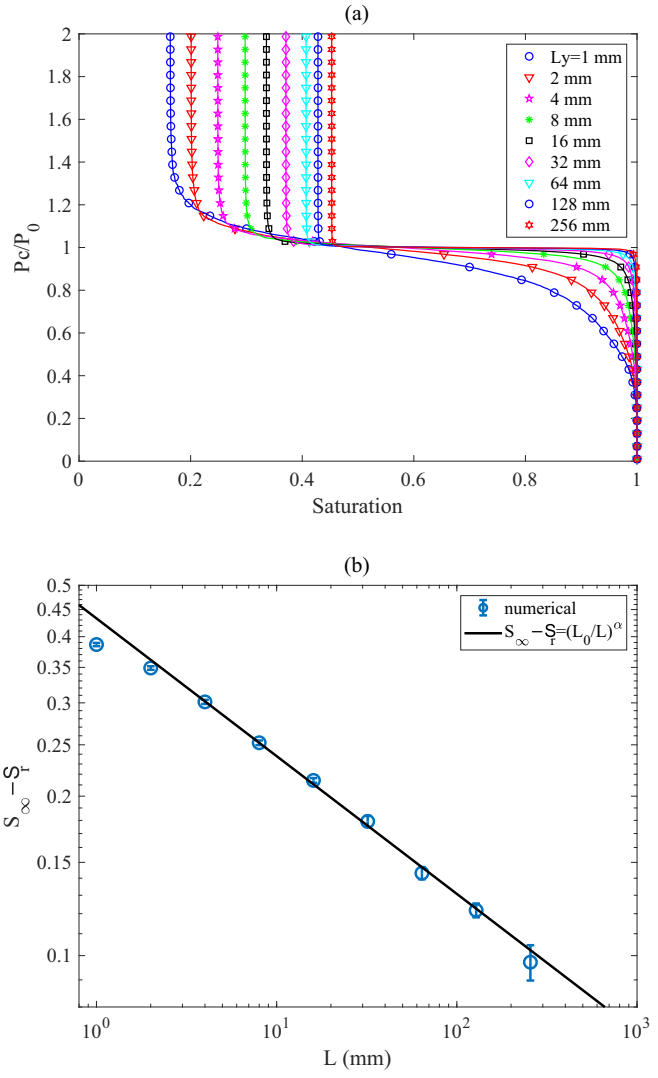

FIG. 8. (a) Pressure-saturation relationship for different sample sizes on square samples. (b) Dependency of the residual saturation on the sample size. The residual saturation is fitted by the relationship $S_r = S_\infty - (L_0/L)^\alpha$, where $S_\infty = 0.55 \pm 0.02$ is the statistical limit of the residual saturation, and $L_0 = (0.04 \pm 0.005)$ mm, and $\alpha = 0.26 \pm 0.02$.

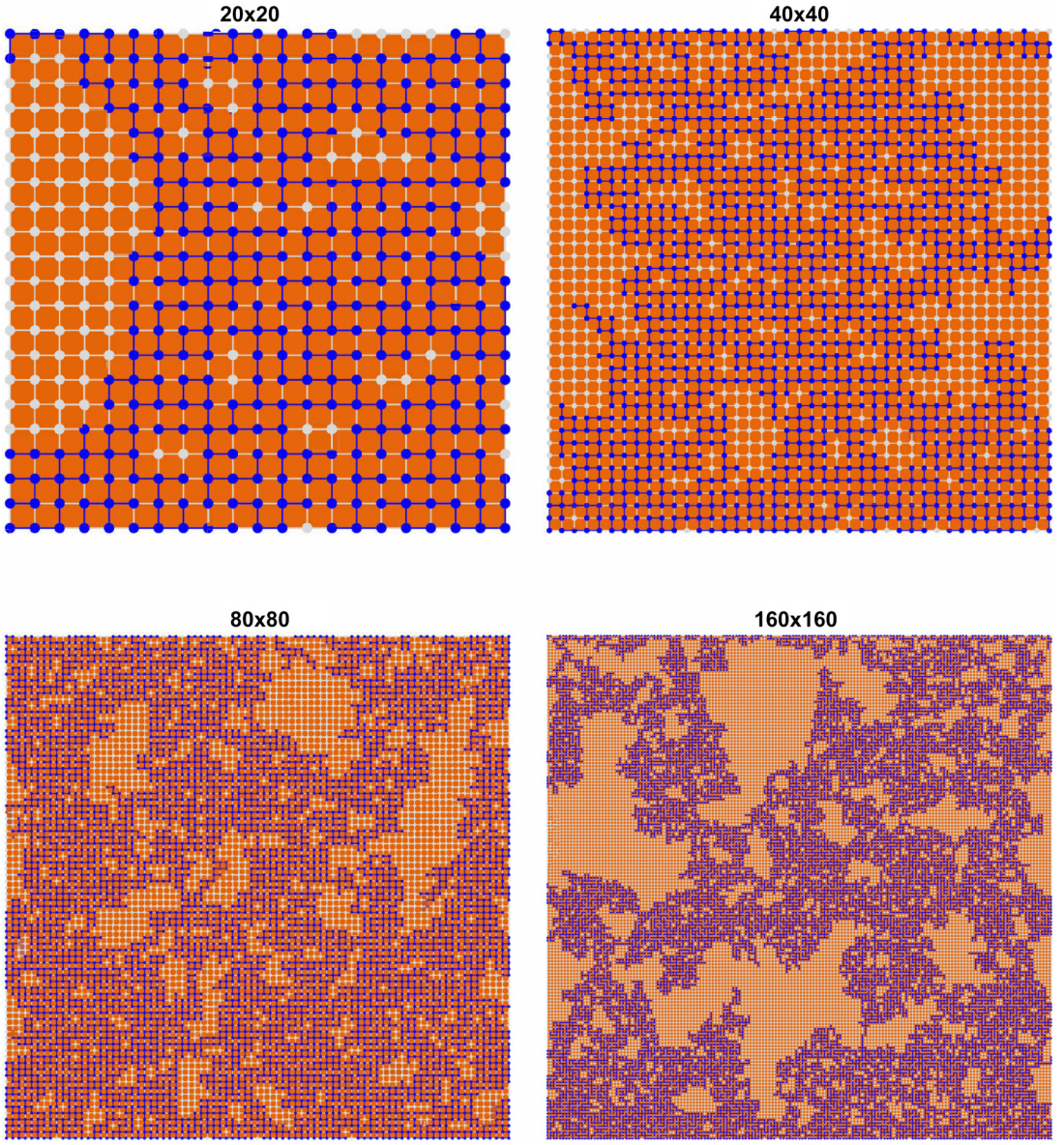

FIG. 9. Final distribution of resident (gray) and invaded (blue) zones for different sample sizes. The dominant clusters of trapped fluid are larger for larger samples, a phenomenon that is characteristic of self-organized criticality systems.

To understand the effect of sample size on residual saturation, we plot the final distribution of fluids for different sample sizes (see Fig. 9 for samples below 0.4 mm size length), the boundary effects are evident, large clusters of trapped fluids appear mostly on the boundary of the fluid. As the sample is enlarged, the relation between perimeter and area decreases, and hence the boundary effects are reduced. However, it is remarkable that the cluster size keeps increasing as the sample size increases. Typically, the size of the largest cluster is of the order of the sample size. There is no apparent average cluster size. This is probably the reason for the ultraslow convergence of the residual saturation as the sample size increases.

VI. DISCUSSION

We presented the results of quasistatic simulations of two immiscible fluids, one displacing the other, in a porous medium. The control parameter of the simulation is the capillary radius. As the capillary pressure increases, the capillary radius decreases, allowing the invaded fluids to access more porous space and hence decreasing the saturation of the resident fluid. We identified two variables to characterize the pressure saturation relation: dimensionless entry pressure and residual saturation. The only parameter affecting the dimensionless entry pressure is the variance of the contact angle, but it is expected that the entry pressure will change for different pore network topologies, apart from the square lattice used in these calculations. The residual saturation seems to be unaffected by either the PTD or the material properties.

Residual saturation depends only on the sample size, and it is expected to depend on the topology of the porous network, which in our case is a simple square lattice. Residual saturation depends neither on material parameters (interfacial tension and wettability) nor on the PTD (median and standard

deviation of the PTD). This is in apparent contradiction to many experimental results showing that decreasing interfacial tension and wettability reduces residual saturation. These discrepancies are due to the way the invasion is performed. In most experiments, including the one to which we compared our results in this paper [8], the invasion of the fluid is carried out using a flow-controlled experiment, while our simulations are controlled by pressure. In a flow-controlled experiment, the pressure drops each time the invaded fluid breaks through a throat, leading to an increase in the capillary radius, according to Eq. (3). This is evident in Fig. 2, where the residual saturation in the pressure-controlled test is lower than that in the flow-controlled test. Thus, these pressure drops reduced the space that the nonwetting fluid can invade compared with the hypothetical case where the pressure is not allowed to drop (and hence the capillary radius does not increase). The residual saturation presented here should be interpreted as the lower bound of all possible saturation values achieved during flow-controlled experiments.

We also note that the limit of the pressure-saturation curve as the sample size increases is particularly restrictive to a steplike function defined by the entry pressure and residual saturation. This step function rules out typical pressure-saturation relations observed in the literature. In particular, experiments in sandstone samples show no plateau in the pressure-saturation relation, but a semilogarithmic relation between pressure and saturation [27]. We should note that these discrepancies are expected, since we focus on the simplest pore network given by the square lattice. The topology of the pore network in sandstone is much more intricate, often exhibiting multiple scales and spatial correlations that are not considered here. A more general description of the pressure-saturation relation will require more diverse pore network topologies and spatial correlation of both materials and geometrical heterogeneities.

We also point out that our simulations are quasistatic and 2D, which imposes restrictions compared with real scenarios. The pore morphology operations are well defined in 2D and 3D. Thus, in principle, the Pore Morphology Method can be extended to 3D simulations, but it will require more computationally demanding calculations. However, time complexity can be reduced by replacing the pores with supervoxels and the throats as connections between these supervoxels. This approach would require replacing the data structure of a 2D image with a 3D undirected graph where nodes are connected by throats. Also, it is possible to add dynamic effects on the Pore Morphology Methods by imposing evolution rules on the dynamics of the capillary radius during the invasion process. This extension will provide an interesting numerical counterpart to advanced voxel-dynamics simulations. Our interest in this paper was quasistatic simulations that provide a computationally efficient calculation of the pressure-saturation relation, which is underexplored in the literature.

VII. CONCLUSIONS

In this paper, we presented an extension of the original Hilper and Miller algorithm to calculate the relationship between capillary pressure and saturation in the multiphase flow of immiscible fluids in porous media. The extension includes effects of wettability and the trapped mechanism, which are not included in the original formulation. The material parameters are given in terms of surface energies that are calculated using DFT. Based on dimensional analysis, we achieved excellent agreement with the experimental results and presented a comprehensive study of the effect of the PTD, material heterogeneity, and sample size. The numerical results were restricted to the simplified topology of the square lattice used in the simulations, but they can be extended to more general topologies.

The most salient result is the emerging criticality that results from finite-size effects. This criticality is reflected in an ultraslow convergence of the residual saturation due to the emergence of clusters of trapped fluids of all sizes, a phenomenon that is typical of Percolation Theory. An extended framework for the pore-scale flow will require the use of percolation theory to identify universal exponents in the pressure-saturation relationship, universality classes for different pore network topologies, and self-similar profiles within these universality classes. Our extended Pore Morphology Method would provide a computationally efficient numerical framework to build a comprehensive Percolation Model for multiphase flow applicable to a wide range of applications.

ACKNOWLEDGMENTS

F.A.M. acknowledges useful discussions within the Integrative-Multiscale Modeling group and with Morteza N. Najafi.

DATA AVAILABILITY

The data that support the findings in this article are not publicly available upon publication because it is not technically feasible and/or the cost of preparing, depositing, and hosting the data would be prohibitive within the terms of this research project. The data are available from the authors upon reasonable request.

[1] M. J. Blunt, *Multiphase Flow in Permeable Media: A Pore-Scale Perspective* (Cambridge University Press, Cambridge, 2017).

[2] E. W. Washburn, The dynamics of capillary flow, Phys. Rev. **17**, 273 (1921).

[3] F. Maggi and F. Alonso-Marroquin, Multiphase capillary flows, Int. J. Multiphase Flow **42**, 62 (2012).

[4] F. Maggi and F. Alonso-Marroquin, Temperature dependence of capillary dynamics: A multiphase and multicomponent adiabatic approach, Phys. Rev. E **88**, 053013 (2013).

[5] F. Maggi, Multiphase capillary rise of multicomponent miscible liquids, Colloids Surf. A **415**, 119 (2012).

[6] Q. Li, K. H. Luo, and X. J. Li, Lattice Boltzmann modeling of multiphase flows at large density ratio with an

improved pseudopotential model, Phys. Rev. E **87**, 053301 (2013).

[7] K. N. Premnath and J. Abraham, Lattice Boltzmann model for axisymmetric multiphase flows, Phys. Rev. E **71**, 056706 (2005).

[8] A. Yiotis, N. Karadimitriou, I. Zarikos, and H. Steeb, Pore-scale effects during the transition from capillary- to viscosity-dominated flow dynamics within microfluidic porous-like domains, Sci. Rep. **11**, 3891 (2021).

[9] M. Hilpert and C. T. Miller, Pore-morphology-based simulation of drainage in totally wetting porous media, Adv. Water Resour. **24**, 243 (2001).

[10] J. C. Fan, J. De Coninck, H. A. Wu, and F. C. Wang, Microscopic origin of capillary force balance at contact line, Phys. Rev. Lett. **124**, 125502 (2020).

[11] See Supplemental Material at http://link.aps.org/supplemental/10.1103/1dw6-m4v2 for standalone code for pore morphology simulation of drainage with trapping.

[12] A. Rabbani, S. Jamshidi, and S. Salehi, An automated simple algorithm for realistic pore network extraction from micro-tomography images, J. Pet. Sci. Eng. **123**, 164 (2014).

[13] M. P. Andersson, M. Bennetzen, A. Klamt, and S. L. S. Stipp, First-principles prediction of liquid/liquid interfacial tension, J. Chem. Theory Comput. **10**, 3401 (2014).

[14] M. P. Andersson, T. Hassenkam, J. Matthiesen, L. V. Nikolajsen, D. V. Okhrimenko, S. Dobberschütz, and S. L. S. Stipp, First-principles prediction of surface wetting, Langmuir **36**, 12451 (2020).

[15] R. Ahlrichs, M. Bar, M. Haser, H. Horn, and C. Kolmel, Electronic-structure calculations on workstation computers - The program system turbomole, Chem. Phys. Lett. **162**, 165 (1989).

[16] A. D. Becke, Density-functional exchange-energy approximation with correct asymptotic behavior, Phys. Rev. A **38**, 3098 (1988).

[17] J. P. Perdew, Density-functional approximation for the correlation energy of the inhomogeneous electron gas, Phys. Rev. B **33**, 8822 (1986).

[18] K. Eichkorn, F. Weigend, O. Treutler, and R. Ahlrichs, Auxiliary basis sets for main row atoms and transition metals and their use to approximate Coulomb potentials, Theor. Chem. Acc. **97**, 119 (1997).

[19] A. Klamt and G. Schüürmann, COSMO: A new approach to dielectric screening in solvents with explicit expressions for the screening energy and its gradient, J. Chem. Soc. Perkin Trans. **2**, 799 (1993).

[20] M. P. Andersson, F. Eckert, J. Reinisch, and A. Klamt, Prediction of aliphatic and aromatic oil-water interfacial tension at temperatures $>100\,^{\circ}$C using COSMO-RS, Fluid Phase Equilib. **476**, 25 (2018).

[21] X. Feng, Y. Deng, and H. W. J. Blöte, Percolation transitions in two dimensions, Phys. Rev. E **78**, 031136 (2008).

[22] C. I. N. Sampaio Filho, J. S. Andrade, Jr., H. J. Herrmann, and A. A. Moreira, Elastic backbone defines a new transition in the percolation model, Phys. Rev. Lett. **120**, 175701 (2018).

[23] D. Wilkinson and J. F. Willemsen, Invasion percolation: A new form of percolation theory, J. Phys. A: Math. Gen. **16**, 3365 (1983).

[24] P. Bak, C. Tang, and K. Wiesenfeld, Self-organized criticality, Phys. Rev. A **38**, 364 (1988).

[25] S. Boggs, *Principles of Sedimentology and Stratigraphy* (Pearson Prentice Hall, Englewood Cliffs, New Jersey, 1996).

[26] C. M. Sperber, B. H. Wilkinson, and D. R. Peacor, Rock composition, dolomite stoichiometry, and rock/water reactions in dolomitic carbonate rocks, J. Geology **92**, 609 (1984).

[27] Z. Cao, G. Liu, H. Zhan, C. Li, Y. You, C. Yang, and H. Jiang, Pore structure characterization of Chang-7 tight sandstone using MICP combined with N_2GA techniques and its geological control factors, Sci. Rep. **6**, 36919 (2016).